

Theoretical systematics in testing the Cosmological Principle with the kinematic quasar dipole

CAROLINE GUANDALIN ¹, JADE PIAT,^{2,1} CHRIS CLARKSON ^{1,3,4} AND ROY MAARTENS ^{3,5,6}

¹*School of Physical & Chemical Sciences, Queen Mary University of London, London E1 4NS, UK*

²*Aix-Marseille University, Marseille, France*

³*Department of Physics & Astronomy, University of Western Cape, Cape Town 7535, South Africa*

⁴*Department of Mathematics and Applied Mathematics, University of Cape Town 7701, South Africa*

⁵*Institute of Cosmology & Gravitation, University of Portsmouth, Portsmouth PO1 3FX, UK*

⁶*National Institute for Theoretical & Computational Sciences (NITheCS), Cape Town 7535, South Africa*

ABSTRACT

The Cosmological Principle is part of the foundation that underpins the standard model of the Universe. In the era of precision cosmology, when stress tests of the standard model are uncovering various tensions and possible anomalies, it is critical to check the viability of this Principle. A key test is the consistency between the kinematic dipoles of the cosmic microwave background and of the large-scale matter distribution. Results using radio continuum and quasar samples indicate a rough agreement in the directions of the two dipoles, but a larger than expected amplitude of the matter dipole. The resulting tension with the radiation dipole has been estimated at $\sim 5\sigma$ for some cases, suggesting a potential new cosmological tension and a possible violation of the Cosmological Principle. However, the standard formalism for predicting the dipole in the 2-dimensional projection of sources overlooks possible evolution effects in the luminosity function. In fact, radial information from the luminosity function is necessary for a correct projection of the 3-dimensional source distribution. Using a variety of current models of the quasar luminosity function, we show that neglecting redshift evolution can significantly overestimate the relative velocity amplitude. While the models we investigate are consistent with each other and with current data, the dipole derived from these, which depends on derivatives of the luminosity function, can disagree by more than 3σ . This theoretical systematic bias needs to be resolved before robust conclusions can be made about a new cosmic tension.

1. INTRODUCTION

The Cosmological Principle (CP), i.e. that the spatial distribution of matter and radiation in the Universe is statistically homogeneous and isotropic on large enough scales, is perhaps the most fundamental assumption in modern cosmology. It is the basis for modelling the Universe using the Friedmann-Lemaître-Robertson-Walker (FLRW) metric (see e.g. Ehlers et al. 1968; Ellis et al. 1983; Stoeger et al. 1995; Clarkson & Maartens 2010; Clarkson 2012). The CP implies that there is a unique cosmic frame defined by observers who measure statistical isotropy and homogeneity of the cosmic microwave background (CMB) and of the matter distribution on sufficiently large scales.

Because Earth observers are not at rest in the cosmic frame, but are moving with a velocity $\mathbf{v}_o^{\text{CMB}}$ rel-

ative to the CMB rest-frame, i.e. the frame in which the CMB dipole vanishes and the CMB is statistically isotropic (Stewart & Sciamia 1967; Peebles & Wilkinson 1968), a dipole measured at $3362.08 \pm 0.99 \mu\text{K}$, which is much larger than the $\ell \geq 2$ multipoles, is used to extract $v_o^{\text{CMB}} = 369.82 \pm 0.11 \text{ km/s}$ towards $(l, b) = (264.021 \pm 0.011, 48.253 \pm 0.005)^\circ$ (Aghanim et al. 2020).

At leading order, the boosted temperature contrast is

$$\tilde{\delta}_T(\mathbf{n}) = \delta_T(\mathbf{n}) + \mathcal{D}_{\text{CMB}} \mathbf{n} \cdot \mathbf{v}_o^{\text{CMB}}, \quad (1)$$

where \mathbf{n} is a unit vector in the direction of observation. Using units with $c = 1$, the dimensionless CMB dipole factor is $\mathcal{D}_{\text{CMB}} = 1$.

The CP requires the large-scale distribution of sources on the sky to have the same dipole – i.e., the relative velocity \mathbf{v}_o extracted from these sources should agree with that from the CMB:

$$\hat{\mathbf{v}}_o \approx \hat{\mathbf{v}}_o^{\text{CMB}}, \quad v_o \approx v_o^{\text{CMB}}. \quad (2)$$

The boosted 2-dimensional number density contrast is

$$\tilde{\delta}_{2D}(\mathbf{n}) = \delta_{2D}(\mathbf{n}) + \mathcal{D} \mathbf{n} \cdot \mathbf{v}_o. \quad (3)$$

The dimensionless number count dipole factor \mathcal{D} is independent of v_o , but it does depend on the sample.

Ellis & Baldwin (1984) estimated the dipole factor for the 2-dimensional projection of radio sources as

$$\mathcal{D}_{EB} = 2 + x(1 + \alpha), \quad (4)$$

in which the power-law indices x and α are constants that determine the number counts per solid angle ($\mathcal{N}_\Omega \propto S_c^{-x}$, with S_c being the flux threshold of the survey) and the flux density of sources in their rest-frame ($S(\nu_{\text{obs}}) \propto \nu_{\text{obs}}^{-\alpha}$) at fixed observed frequency ν_{obs} . This is potentially the most powerful consistency test of the CP, but it faces major observational obstacles.

First, the galaxy sample needs to cover a wide sky area and a deep redshift range, with a high number density. High redshifts are required to extract the cosmic dipole – and the lowest redshift sources need to be removed to avoid nonlinear contamination of the cosmic signal (Tiwari & Nusser 2016; Bengaly et al. 2019). Second, there are well-known systematic errors facing measurements of large-scale features (effects of the mask, instrumental/survey systematics, stellar contamination, etc.). In this paper, we focus on a key theoretical systematic error that arises when the dimensionless dipole factor \mathcal{D} is estimated without using radial information.

Different groups have applied Eq. (4) to extract the relative velocity from the measured dipole in wide-area radio continuum surveys (see e.g. Blake & Wall 2002; Gibelyou & Huterer 2012; Rubart & Schwarz 2013; Tiwari et al. 2015; Ghosh et al. 2016; Colin et al. 2017; Bengaly et al. 2018). A general conclusion of these analyses is that the dipole direction is typically consistent with that of the CMB, but the relative velocity amplitude is significantly larger:

$$\hat{\mathbf{v}}_o^{\text{EB}} \approx \hat{\mathbf{v}}_o^{\text{CMB}}, \quad v_o^{\text{EB}} > v_o^{\text{CMB}}. \quad (5)$$

Recently, one of the most thorough analyses has used the very large CatWISE2020 sample of quasars to apply the Ellis-Baldwin test (Secrest et al. 2021, 2022). Their conclusion reinforces Eq. (5), finding a tension with the CMB velocity amplitude at $\sim 5\sigma$.

In this work, we do not make any measurement of the dipole from data. Instead, our aim is to extend the pioneering analysis of Dalang & Bonvin (2022), who first showed that corrections to the Ellis-Baldwin approximation could be significant in the presence of parameter evolution. We investigate the impact that different quasar luminosity function (QLF) models have on the

predicted amplitude of the kinematic dipole and how the errors on the measurements propagate to \mathcal{D} . In Sec. 2, we review the theoretical predictions for the expected kinematic dipole amplitude in 3-dimensions, \mathcal{D}_{3D} , and how it can be projected into the 2D dipole factor \mathcal{D} of Eq. (3); in Sec. 3, we introduce the QLF data and the theoretical modelling used for the fits; in Sec. 4, we describe the likelihood employed in the Markov chain Monte Carlo (MCMC) analyses, together with the criterion used to assess the goodness of fit; finally, we present our results in Sec. 5 and conclude in Sec. 6.

2. CORRECTION TO THE STANDARD DIPOLE

In all of the results characterised by Eq. (5), the dipole is measured and then Eq. (4) is used to extract the relative speed. However, \mathcal{D}_{EB} assumes that radial information can be neglected. In reality, \mathcal{D} is a radial projection of the 3-dimensional dipole factor (Maartens et al. 2018)

$$\mathcal{D}_{3D} = 2 + \frac{\dot{\mathcal{H}}}{\mathcal{H}^2} + \frac{2}{r\mathcal{H}} - \frac{5s}{r\mathcal{H}} - b_e, \quad (6)$$

which can be derived from linear perturbations¹.

In this redshift-dependent factor, the first 3 terms on the right are purely cosmological (where r is the comoving line-of-sight distance); the last 2 terms contain the magnification (s) and evolution (b_e) biases. These quantities depend on the luminosity function Φ of the sample through the background comoving number density (in the source frame):

$$n(z, M_c) = \int_{-\infty}^{M_c(z)} dM \Phi(z, M). \quad (7)$$

The absolute magnitude of a source (corresponding to its intrinsic luminosity) is given by

$$M = m(z) - \mu(z) - K(z), \quad (8)$$

where m is the apparent magnitude measured at redshift z (corresponding to observed flux), μ is the distance modulus (defined by the background luminosity distance) and K is the K -correction. The apparent magnitude cut of the survey m_c leads to an absolute threshold $M_c(z)$ that depends on redshift via Eq. (8). The magnification and evolution biases become (Challinor &

¹ There is also an intrinsic dipole sourced by primordial perturbations (Tiwari & Nusser 2016; Nadolny et al. 2021), which is not relevant for our discussion.

Lewis 2011; Alonso et al. 2015; Maartens et al. 2021)

$$s(z, M_c) = \frac{\partial \log n(z, M_c)}{\partial M_c} = \frac{1}{\ln 10} \frac{\Phi(z, M_c)}{n(z, M_c)}, \quad (9)$$

$$b_e(z, M_c) = -\frac{\partial \ln n(z, M_c)}{\partial \ln(1+z)}$$

$$= -\frac{(1+z)}{n(z, M_c)} \int_{-\infty}^{M_c(z)} dM \left. \frac{\partial \Phi(z, M)}{\partial z} \right|_M, \quad (10)$$

in which s determines whether sources are included or excluded in the sample due to lensing convergence and b_e describes the deviation of the comoving number density of sources from the conserved case ($b_e = 0$). Note the partial redshift derivative in b_e must be taken at fixed magnitude M_c .

The observed source number density \mathcal{N} (number per redshift per solid angle), is not the same as the number density n (number per comoving volume) measured at the source (Challinor & Lewis 2011; Bonvin & Durrer 2011; Alonso et al. 2015; Maartens et al. 2018, 2021). At the background level, these quantities are related by

$$\mathcal{N} = \frac{dN}{dz d\Omega} = \frac{r^2}{(1+z)\mathcal{H}} n, \quad (11)$$

where N is the number of sources, which is the same in the observer and source frames: $dN = \mathcal{N} dz d\Omega = n dV$, with V the comoving volume. The observed number density projected on the sky becomes

$$\mathcal{N}_\Omega = \int_0^\infty dz \mathcal{N}(z). \quad (12)$$

The 2D dipole factor is found by projecting Eq. (6) along the radial direction, weighted by the number counts (Nadolny et al. 2021; Dalang & Bonvin 2022)²:

$$\mathcal{D} = \int_0^\infty dz f(z) \mathcal{D}_{3D}(z) \quad \text{where} \quad f(z) = \frac{\mathcal{N}(z)}{\mathcal{N}_\Omega}. \quad (13)$$

The result is

$$\mathcal{D} = \mathcal{D}_{\text{cosmo}} + \mathcal{D}_{\text{mag}} + \mathcal{D}_{\text{evol}}, \quad (14)$$

where³

$$\mathcal{D}_{\text{cosmo}} = \int_0^\infty dz f \left[2 + \frac{2}{r\mathcal{H}} + \frac{\dot{\mathcal{H}}}{\mathcal{H}^2} \right], \quad (15)$$

$$\mathcal{D}_{\text{mag}} = -2 \int_0^\infty dz f \frac{x}{r\mathcal{H}} \quad \text{with} \quad x = \frac{5}{2} s, \quad (16)$$

$$\mathcal{D}_{\text{evol}} = - \int_0^\infty dz f b_e. \quad (17)$$

² In these papers, their \mathcal{D}_{kin} equals our $\mathcal{D} v_o$.

³ Eq. (16) corrects Eq. (43) of Dalang & Bonvin (2022), which accounts for differences in our results.

For a constant magnification bias, x corresponds to the Ellis-Baldwin parameter in Eq. (4), but in general x evolves with redshift. Note that \mathcal{D} in the form of Eqs. (14) – (17) does not depend on the source spectral index α , which can vary significantly across the sample (Carballo et al. 1999; Secrest et al. 2021). Instead, the dependence is on the evolution bias b_e , which is unique for the sample. This is an important feature and it arises from the fact that the absolute magnitude cut $M_c(z)$ does not depend on α at fixed redshift. By contrast, the absolute magnitude cut does depend on α at fixed distance r (for a detailed discussion, see Dalang & Bonvin 2022).

The Ellis-Baldwin formula is an approximation to Eq. (13), $\mathcal{D}_{\text{EB}} = \mathcal{D} + \Delta\mathcal{D}$, and this correction does not affect the dipole direction. The dipole amplitude is extracted directly from data and it corresponds to the dipole factor times the relative speed:

$$\mathcal{D}_{\text{EB}} v_o^{\text{EB}} = \mathcal{D} v_o. \quad (18)$$

When Eq. (13) is used for the dipole factor \mathcal{D} , then we extract the correct relative speed v_o from the measurement. However, if we use the Ellis-Baldwin approximation \mathcal{D}_{EB} , then we extract an estimate of the relative speed that may differ from v_o : $v_o^{\text{EB}} = v_o + \Delta v_o$. For example, if the relative speed is overestimated, i.e., $v_o^{\text{EB}} > v_o$, then \mathcal{D}_{EB} underestimates \mathcal{D} , since $\Delta v_o/v_o = -\Delta\mathcal{D}/\mathcal{D}$ by Eq. (18).

3. DATA

We consider measurements of the quasar luminosity function (QLF) as given by Palanque-Delabrouille et al. (2016) (PD2016 hereafter). The sample has 13876 quasars: 7900 are identified via the time variability of their fluxes (Schmidt et al. 2010; Palanque-Delabrouille et al. 2011) within the Sloan Digital Sky Survey (SDSS) photometric $\{u, g, r, i, z\}$ bands; 5976 are spectroscopically identified in the Stripe 82 region, which does not rely on the time-variability method.

This data is part of the extended Baryon Oscillation Spectroscopic Survey (eBOSS) of SDSS-IV and it can be found in Table A.1 of PD2016. Each SDSS magnitude is corrected for Galactic extinction (see PD2016, Sec. 3) and the magnitude limit is $g_{\text{dered}} = 22.5$ for the dereddened g band.

3.1. Theoretical modelling

There are two main sources of uncertainties in the number counts of quasars: the very bright end of the sample is highly uncertain due to the small number of sources, while the very faint end is limited by the survey strategy. Therefore, both ends of the luminosity function show large uncertainties. Hence, we adopt a double

power law fit for the comoving space density of quasars (Boyle et al. 2000; Croom et al. 2004, 2009; Ross et al. 2013),

$$\Phi(z, M_g) = \frac{\Phi_*}{10^{0.4(a+1)(M_g - M_*)} + 10^{0.4(b+1)(M_g - M_*)}}. \quad (19)$$

Above, Φ_* is a normalisation factor related to the characteristic number density of quasars; M_* is the break magnitude, associated with their characteristic luminosity; a and b describes, respectively, the behaviour of the bright and faint ends and

$$M_g(z) = m_g - \mu(z) - [K(z) - K(z = 2)] \quad (20)$$

is the absolute magnitude corresponding to the observed apparent magnitude m_g in the g band after the K -correction

$$K(z) = -2.5(1 + \alpha_v) \log_{10}(1 + z), \quad \alpha_v \simeq -0.5 \quad (21)$$

has been applied (Croom et al. 2009; PD2016).

The number density of quasars has a strong redshift dependence and there are different ways in which the QLF can evolve: (a) it can be due to a change in the luminosity as a function of redshift; in this pure-luminosity evolution (PLE) case, the *characteristic* number density remains constant, but the break magnitude (associated with the break luminosity) changes with time; (b) it can be due to a pure-density evolution (PDE), where the luminosities of individual sources remain constant, but the number density changes with time; (c) it can be a combination of the two cases, i.e. a luminosity evolution and a density evolution (LEDE). Finally, a redshift dependence may also appear in the bright- and faint-end slopes (Ross et al. 2013, and references therein).

Since the QLF is very uncertain, one of the aims of this work is to investigate different evolution models for Φ_* , M_* , a and b , and to assess the impact on the final kinematic dipole \mathcal{D} . In Appendix A, the models we considered are described in full details. They are (Croom et al. 2004; Ross et al. 2013; PD2016):

- PLE – the QLF redshift evolution comes from the break magnitude M_* . The pivot scale $z_p = 2.2$ is introduced to allow the bright- and faint-end slopes to vary for low ($z < z_p$) and high ($z > z_p$) redshifts.
- LEDE – both luminosity and number density vary with time. We consider a linear (LEDE₇) and quadratic (LEDE₈) redshift dependence on the break magnitude $M_*(z)$ and these two models are extended by allowing both slopes to evolve linearly with redshift (LEDE₇₊₂ and LEDE₈₊₂).

- PLE+LEDE – it combines the PLE functional form for $z < z_p$, and the LEDE₇ model for $z > z_p$. We allow the bright slope a to evolve with redshift.

4. METHOD

4.1. Maximum likelihood

We consider a maximum-likelihood approach to sample the parameter space of the models of Sec. 3.1. Because the QLF is estimated from the number counts of quasars inside each magnitude bin, its error can be approximately modelled by Poissonian error bars. Therefore, we model the log-likelihood function as (Pozzetti et al. 2016)

$$\ln \mathcal{L} = \sum_{i,j} \frac{\Delta_{i,j}^2}{\sigma_{i,j}^2}, \quad (22)$$

In this equation, $\Delta_{i,j}^2 \equiv 1 - \Phi_\theta(z_i, M_j)/\Phi_{\text{obs}}(z_i, M_j) + \ln[\Phi_\theta(z_i, M_j)/\Phi_{\text{obs}}(z_i, M_j)]$, $\sigma_{i,j}^2 = 1/N_{\text{obs}}(z_i, M_j)$, Φ_θ is given by the model of Eq. (19). Finally, Φ_{obs} and N_{obs} are, respectively, the corresponding QLF measurements and the angle averaged number counts in each redshift z_i and magnitude M_j bin. To maximise Eq. (22), we used the MCMC sampler `emcee` (Foreman-Mackey et al. 2013) with flat priors for the fitting parameters.

4.2. Goodness of fit

To assess the goodness of fit of the models considered in Sec. 3.1 to the eBOSS data, in Table 2 we present the Bayesian information criterion (BIC),

$$\text{BIC} = p \ln(n) - 2 \ln \mathcal{L}^*, \quad (23)$$

in which p is the number of parameters in the model, n is the number of data points used and $\ln \mathcal{L}^*$ is the log-likelihood computed at the best-fitting values (e.g. Liddle 2004).

5. RESULTS

We fitted the QLF models described in the Appendix A to the eBOSS data. In Table 1, we show the mean of 5000 samples and the 1σ constraints obtained for the amplitude of the kinematic dipole. The posteriors for the QLF are presented in Table 2, together with their goodness of fit.

In Figure 1, the number density, evolution and magnification biases derived from the best-fitting QLF are shown, after assuming a flat Λ CDM model with parameters $h = 0.679$, $n_s = 0.9681$, $\sigma_8 = 0.8154$, $\Omega_m = 0.3065$ and $\Omega_b h^2 = 0.02227$ (Ade et al. 2016) (same cosmology employed in PD2016 for the distance modulus μ). To assess the dependence of our results on the fiducial cosmology used to compute Eq. (14), in Table 1 the constraints obtained with a flat w CDM cosmology with parameters

Table 1. 1σ constraints for $\mathcal{D}_{\text{kin}} = \mathcal{D} v_o^{\text{CMB}}/c$, in units of 10^{-3} for a better visualisation, obtained from 5000 MCMC samples for each QLF model. The results are shown for the fiducial Planck 2015 and the w CDM cosmologies. We also present the constraints obtained with different absolute magnitude thresholds: $M_{c,g} = -25$ (encompasses all redshift bins), $M_{c,g} = -24.6$ (neglects the last redshift bin) and a varying $M_c(z)$. The effect of neglecting the redshift evolution of the magnification and evolution biases (Eq. 24) for the fiducial Planck 2015 cosmology and absolute magnitude threshold $M_{c,g} = -25$ are shown in the last column.

| | $\mathcal{D}_{\text{kin}} [10^{-3}]$ | | | | | |
|---------------------|--------------------------------------|------------------------|------------------------|------------------------|--|------------------------|
| | w CDM | Planck 2015 | | | + $\{b_e^{\text{eff}}, s^{\text{eff}}\}$ | |
| | $M_{c,g} = -25$ | $M_{c,g} = -25$ | $M_{c,g} = -24.6$ | $M_{c,g} = M_{c,g}(z)$ | $M_{c,g} = -25$ Best fit | Chains |
| PLE | $0.72_{-0.10}^{+0.10}$ | $0.75_{-0.10}^{+0.10}$ | $1.42_{-0.10}^{+0.10}$ | $0.39_{-0.05}^{+0.05}$ | $0.8129_{-0.0004}^{+0.0004}$ | $0.84_{-0.12}^{+0.12}$ |
| LEDE ₇ | $0.32_{-0.03}^{+0.03}$ | $0.34_{-0.03}^{+0.03}$ | $0.90_{-0.04}^{+0.04}$ | $0.53_{-0.06}^{+0.06}$ | $0.4859_{-0.0009}^{+0.0009}$ | $0.28_{-0.04}^{+0.04}$ |
| LEDE ₇₊₂ | $0.59_{-0.06}^{+0.06}$ | $0.62_{-0.06}^{+0.06}$ | $1.14_{-0.06}^{+0.06}$ | $0.67_{-0.05}^{+0.05}$ | $0.7206_{-0.0007}^{+0.0007}$ | $0.75_{-0.07}^{+0.07}$ |
| LEDE ₈ | $0.39_{-0.03}^{+0.03}$ | $0.42_{-0.03}^{+0.03}$ | $1.01_{-0.04}^{+0.04}$ | $0.44_{-0.06}^{+0.06}$ | $0.5396_{-0.0009}^{+0.0009}$ | $0.38_{-0.04}^{+0.04}$ |
| LEDE ₈₊₂ | $0.40_{-0.05}^{+0.03}$ | $0.42_{-0.05}^{+0.03}$ | $0.99_{-0.04}^{+0.04}$ | $0.50_{-0.07}^{+0.07}$ | $0.5330_{-0.0009}^{+0.0009}$ | $0.42_{-0.07}^{+0.05}$ |
| PLE+LEDE | $0.60_{-0.08}^{+0.08}$ | $0.62_{-0.08}^{+0.08}$ | $1.31_{-0.09}^{+0.08}$ | $0.47_{-0.05}^{+0.05}$ | $0.7237_{-0.0007}^{+0.0007}$ | $0.77_{-0.11}^{+0.11}$ |

$h = 0.72$, $n_s = 0.963$, $\sigma_8 = 0.852$, $\Omega_m = 0.275$, $\Omega_b h^2 = 0.02258$, $\Omega_{\text{DE}} = 0.725$, and $w = -1.2$ (Rasera et al. 2022) are also shown. As one can see in Table 1, the constraints are robust against this change.

We considered different absolute magnitude thresholds: $M_{c,g}(z_8) = -25$, corresponding to the apparent magnitude cut $g_{\text{dered}} = 22.5$ at the centre $z_8 = 3.75$ of the last redshift bin (e.g. Wang et al. 2020), $M_{c,g}(z_7) = -24.6$, corresponding to g_{dered} at $z_7 = 3.25$ and a varying $M_{c,g}(z)$, obtained from Eq. (20) at each redshift used to compute $n(z, M_c)$, $b_e(z, M_c)$ and $s(z, M_c)$.

In Figure 2, we show the impact of the magnitude cut M_c on the results (first, second and fourth panels). By fixing a threshold such as $M_c = -25$, we discard data at lower redshifts (see Figure 3). Hence, the number density increases by allowing larger values for M_c . By considering $M_c = -24.6$, we neglect the last redshift bin in the analysis to avoid adding sources too faint to be seen at the highest z -bin. Thus, we are probing the kinematic dipole with lower- z sources and this shifts \mathcal{D} to larger values as the integration range changes (fourth panel of Figure 2). Most of the impact comes from the $\mathcal{D}_{\text{cosmo}}$ term.

The evolution bias derived from the LEDE₇, LEDE₈ and LEDE₈₊₂ models are very similar at high redshifts. While the evolution bias is rather consistent among different models, the magnification bias has a larger dependence on the QLF. However, the contributions coming from Eq. (16) exhibit a smaller dispersion due to the $1/r\mathcal{H}$ suppression in \mathcal{D}_{mag} . The contributions from the evolution term (Eq. 17) are more sensitive to the differences in the QLF. This is manifested in the final 2D amplitude \mathcal{D} : LEDE₇, LEDE₈ and LEDE₈₊₂ agree within $\sim 1\sigma$, while the LEDE₇₊₂, PLE and PLE+LEDE have a $\sim 1\sigma$ consistency among each other.

We also tested the robustness of our results against the minimum redshift considered: the values presented in Table 1 were obtained by numerically integrating Eqs. (15) - (17) from $z_{\text{min}} \approx 0$ to $z_{\text{max}} = 4$ (the maximum redshift of the sample). Because the number of sources below $z = 0.68$ (minimum redshift) is very small, we find no significant changes in the constraints for the dipole amplitude. Still, it is worth stressing the fact that the intrinsic dipole is considerable for low- z sources; therefore, in principle it is better to remove $z \lesssim 0.5$ to avoid nonlinear contamination in real data (Tiwari & Nusser 2016; Bengaly et al. 2019).

Finally, considering the Planck 2015 cosmology and $M_{c,g} = -25$, we neglect the redshift evolution of the magnification and evolution biases, i.e.

$$s^{\text{eff}} = \int dz f(z)s(z) \quad \text{and} \quad b_e^{\text{eff}} = \int dz f(z)b_e(z). \quad (24)$$

This has been done for (a) each one of the 5000 chains, i.e. calculating $f(z)$, $s(z)$ and $b_e(z)$ for each chain and then projecting along z , and (b) by fixing them to the best-fitting functions. In the first case, the results agree within the 1σ errors; for the second case, however, the amplitudes are overestimated by more than 3σ for the LEDE₇ and LEDE₈ models.

Our results summarise the expected dipole in the number counts of quasars from a pure kinematic origin. They are all above the intrinsic dipole expected from the clustering anisotropy (grey-dashed line in Figure 2), which comes from fluctuations in the number density around the FLRW metric (Nadolny et al. 2021) and can be distinguished given the 1σ errors.

6. CONCLUSIONS

In this work, we extended the analysis of Dalang & Bonvin (2022) to accommodate the uncertainties on

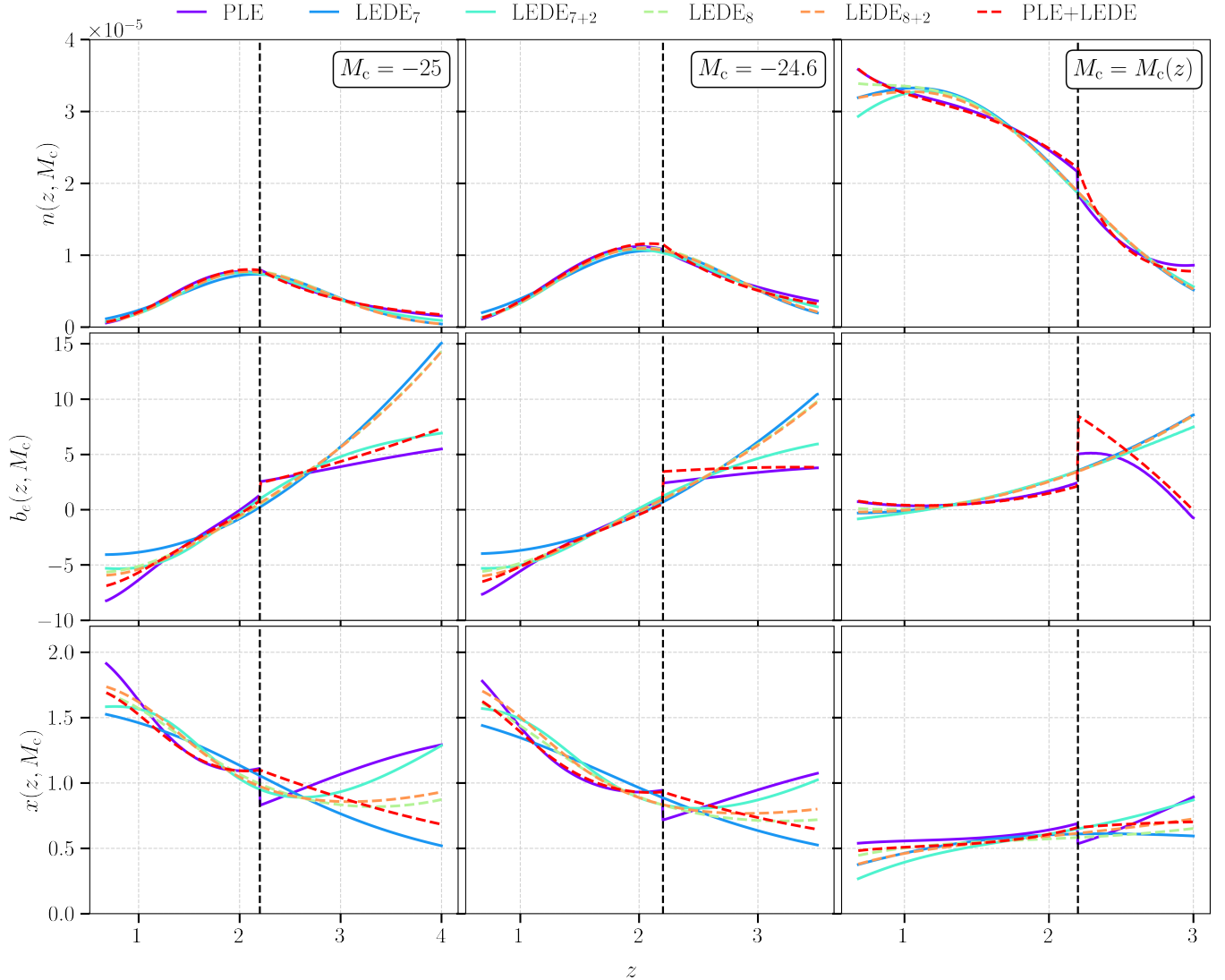


Figure 1. Comoving number density (*top*), evolution (*middle*) and magnification (*bottom*) biases derived from the QLF with different absolute magnitude thresholds, assuming Planck 2015 cosmology (Ade et al. 2016). Vertical dashed line marks the pivot redshift $z_p = 2.2$ entering both PLE and PLE+LEDE models.

both magnification s and evolution b_e biases (Eqs. 9 and 10 respectively). We employed a maximum-likelihood approach to 6 different models used to fit the QLF, Eq. (19), from which the number density $n(z)$ (Eq. 7), $s(z)$ and $b_e(z)$ could be derived (Wang et al. 2020), finding that models of QLF have non-negligible impact on the biases (Figure 1). From the MCMC chains obtained for these quantities, we computed the amplitude of the cosmic kinematic dipole \mathcal{D} (Eq. 14), finding that the QLF introduces a large model dependence on \mathcal{D} . In some cases, a $\sim 3\sigma$ tension on the dipole amplitude computed with different models (Figure 2) is found.

The constraints on \mathcal{D} are robust under a change of fiducial cosmology (see Table 1). Neglecting data from the last redshift bin does not degrade the constraints, as

the 1σ error bars on \mathcal{D} are of the same order, although the amplitude shifts to larger values as we increase the magnitude threshold of the survey, $M_{c,g}$, mainly due to a different redshift range.

To analyse the impact of neglecting the redshift evolution of the magnification and evolution biases, we considered effective values, s^{eff} and b_e^{eff} (Eq. 24), by integrating these quantities over the redshift range of the sample. We computed s^{eff} and b_e^{eff} for each MCMC sample, finding a shift in the expected amplitude within the 1σ region of the cases in which the redshift evolution is accounted for. We also fixed the biases and the normalised redshift distribution $f(z)$ to the best-fitting functions, finding tight constraints around high values of \mathcal{D} . This points to an overestimation of the 2D ampli-

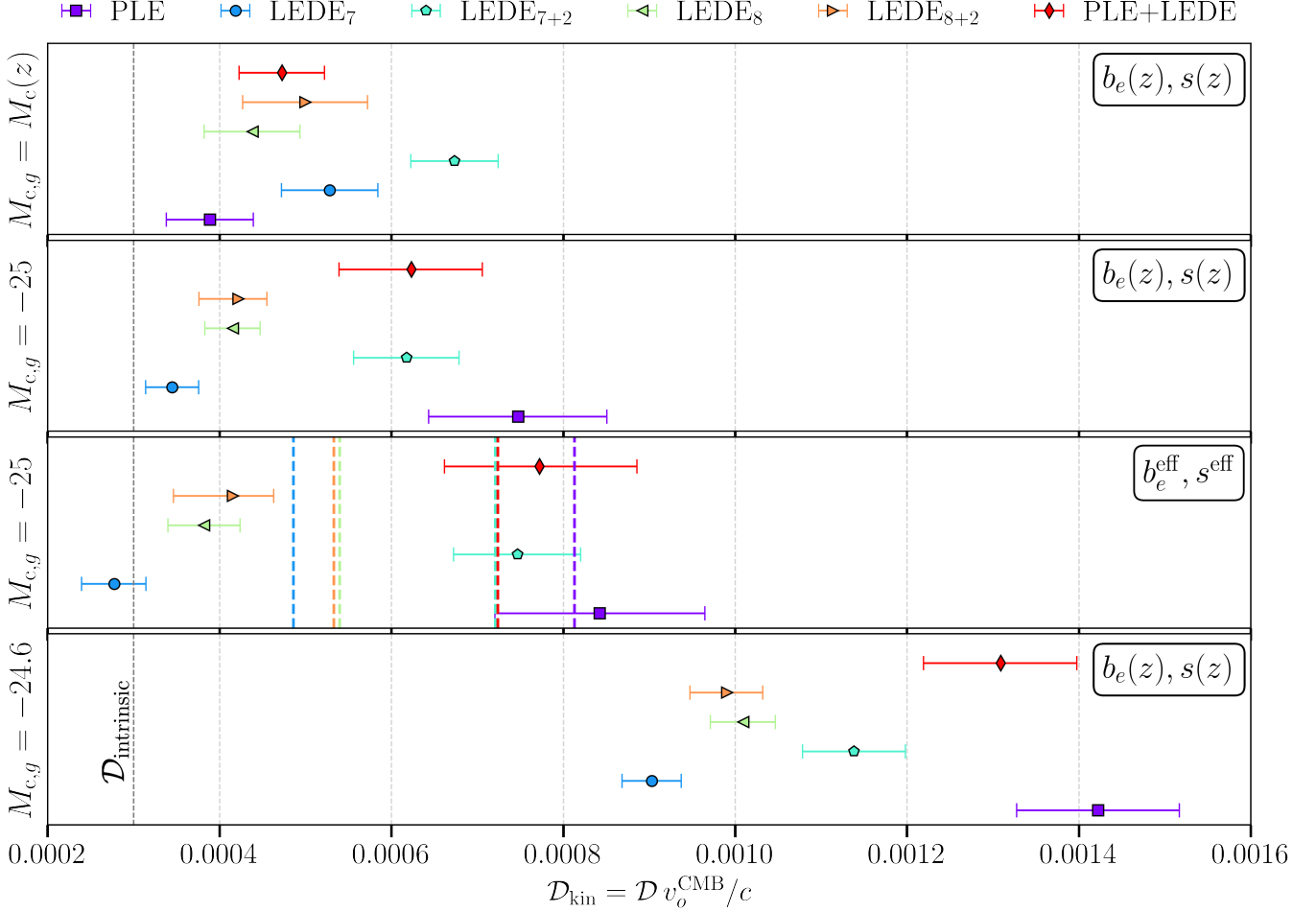


Figure 2. 1σ constraints for $\mathcal{D}_{\text{kin}} = \mathcal{D} v_o^{\text{CMB}}/c$, obtained from 5000 MCMC samples for each QLF model, assuming Λ CDM cosmology. The grey-dashed vertical line is merely a reference for the intrinsic dipole (Dalang & Bonvin 2022). The first panel (top to bottom) shows the analysis for a varying magnitude threshold $M_c(z)$, i.e. the corresponding absolute magnitude for $g = 22.5$ at each redshift used to compute $n(z)$ (Eq. 7). The second and third panels correspond to a fixed magnitude threshold given by the last redshift bin (see Figure 3 for illustration) and the last panel shows the constraints by neglecting the last z -bin (i.e. considering data in the range $0 \lesssim z < 3.5$). In the third panel, the constraints were obtained without accounting for the redshift evolution (Eq. 24) of the magnification and evolution biases. The *points with error bars* show the constraints when we project $s(z)$ and $b_e(z)$ in redshift for each MCMC sample and the *dashed vertical lines* correspond to the projection when we use the best-fitting functions. The error bars for the latter case are negligible (see Table 1). As evident from these results, different models of the QLF lead to amplitudes of \mathcal{D} that can be in $\sim 3\sigma$ tension. By comparing the second and third panels, we see that neglecting the redshift evolution of $s(z)$ and $b_e(z)$ lead to significant tensions in some cases. In the last panel, we neglect data from the last redshift bin. While the 1σ constraints are of the same order, the amplitude shift to larger values mainly due to the different redshift range used to obtain \mathcal{D} .

tude when the redshift evolution is neglected in quantities that evolve with z .

The model dependence introduced by the QLF in the dipole amplitude contrasts significantly with the results of Ellis & Baldwin (1984), which has been used as a model-independent null hypothesis to test the validity of the Cosmological Principle. As we have shown, in the absence of a single description of the quasar evolution, and with a variety of models being equally good fits

to the data, the Cosmological Principle test using the quasar dipole is much less trivial than has been assumed.

Finally, since the CatWISE2020 is an infrared survey, no conclusions from our work can be directly extrapolated to the results of Secrest et al. (2022): first, there is no reason for the QLF obtained for eBOSS quasars to be directly applicable to their quasar sample and second, it is possible that α (Eq. 4) could indeed have a negligible redshift dependence for that particular sample. However, given the results of our alternative ap-

proach, we stress that in-depth studies of the spectral index α of quasars are crucial: if it varies with redshift, then the projected α could introduce a statistically significant bias in the amplitude of the kinematic dipole and could depend sensitively on the modelling, as well as other assumptions used in the Ellis-Baldwin approach. Because the magnification and evolution biases are found to vary with redshift for all the models considered for the eBOSS quasars, with significant implications for the dipole amplitude, it is paramount to investigate whether evolution effects are also present in the data considered for the analyses leading to Eq. (5) before strong claims about violation of the Cosmological Principle are validated.

¹ We thank Charles Dalang, Carolina Queiroz, José Luis
² Bernal, Mike Shengbo Wang and Phil Bull for discus-
³ sions and comments. CG and CC are supported by
⁴ the UK Science & Technology Facilities Council Con-
⁵ solidated Grant ST/P000592/1. RM is supported by
⁶ the South African Radio Astronomy Observatory and
⁷ the National Research Foundation (Grant No. 75415).

Facilities: This work uses data from the extended Baryon Oscillation Spectroscopic Survey of the Sloan Digital Sky Survey (SDSS-IV/eBOSS), as extracted from Table A.1 of PD2016.

Software: We made extensive use of `emcee` (Foreman-Mackey et al. 2013), `CLASS` (Blas et al. 2011), `numpy` (Harris et al. 2020), `scipy` (Virtanen et al. 2020), and `matplotlib` (Hunter 2007).

APPENDIX

A. QUASAR LUMINOSITY FUNCTION MODELS

In this Appendix we describe the QLF models considered for the main analysis.

A.1. *Pure-Luminosity Evolution (PLE)*

In this model, the luminosity function evolves solely through a redshift evolution in the break magnitude M_* (Boyle et al. 2000; PD2016):

$$M_*(z) = M_*(z_p) - 2.5 [k_1(z - z_p) + k_2(z - z_p)^2]. \quad (\text{A1})$$

Early studies showed a preference for this model, but deeper data revealed deviations from the PLE model at redshifts larger than $z \gtrsim 2$ (Ross et al. 2013) for $z_p = 0$. Therefore, the bright- and faint-end slopes are allowed to vary for low ($z < z_p$) and high ($z > z_p$) redshifts, $a_{\{l,h\}}$, $b_{\{l,h\}}$, and so are the k_1 and k_2 . The pivot redshift is $z_p = 2.2$. In this model, there are 10 free parameters: $\{a_l, b_l, a_h, b_h, k_{1,l}, k_{2,l}, k_{1,h}, k_{2,h}, M_*(z_p), \log_{10} \Phi_*\}$ (PD2016).

A.2. *Luminosity and Density Evolution (LEDE)*

We also consider the case in which both the luminosity and number density vary with time: the so-called Luminosity Evolution + Density Evolution (LEDE) model (Ross et al. 2013; PD2016). We analyse this particular case motivated by the fact that the discontinuity present at the pivot redshift $z_p = 2.2$ for the derived quantities is removed, thus leading to a smooth behaviour with redshift for the derived quantities.

We will take the density and magnitude evolution respectively as

$$\log_{10} \Phi_*(z) = \log_{10} \Phi_*(z_p) + c_1(z - z_p) + c_2(z - z_p)^2, \quad (\text{A2})$$

$$M_*(z) = M_*(z_p) + c_3(z - z_p). \quad (\text{A3})$$

Because it has 7 free parameters $\{a, b, c_1, c_2, c_3, \log_{10} \Phi_*(z_p), M_*(z_p)\}$, we will label it LEDE₇ hereafter. Notice that, in this case, the bright- and faint-ends are fixed for the whole redshift range: $a(z) = a$, $b(z) = b$.

We shall also consider a quadratic redshift dependence for the break magnitude (Boyle et al. 2000; Croom et al. 2009):

$$M_*(z) = M_*(z_p) + c_3(z - z_p) + c_4(z - z_p)^2. \quad (\text{A4})$$

We dub this case LEDE₈ as it contains 8 free parameters: $\{a, b, c_1, c_2, c_3, c_4, \log_{10} \Phi_*(z_p), M_*(z_p)\}$. Again, a and b are fixed.

Finally, we consider extensions to LEDE₇ and LEDE₈, in which both slopes are allowed to evolve linearly with redshift:

$$a(z) = a(z_p) + c_a(z - z_p), \quad b(z) = b(z_p) + c_b(z - z_p). \quad (\text{A5})$$

These will be called, respectively, LEDE₇₊₂ and LEDE₈₊₂, where the +2 indicates the extra c_a and c_b parameters introduced for the redshift evolution in the bright- and faint-ends.

A.3. Composite Evolution Model (PLE+LEDE)

We also consider the combination of the PLE functional form for $z < z_p$, and the LEDE₇ model for $z > z_p$ (PD2016). Other combinations with LEDE₈ and redshift dependencies of the slopes are possible. However, we focus on this particular combination of PLE + LEDE₇ and allow only the bright slope to evolve with redshift: $\alpha(z) = \alpha(z_p) + c_a(z - z_p)$. In total, we have 10 free parameters: $\{\alpha(z_p), \beta, k_1, k_2, c_1, c_2, c_3, c_a, \log_{10} \Phi_*(z_p), M_*(z_p)\}$.

B. MCMC RESULTS

In Table 2, we present the best-fitting values for the QLF obtained for the 6 models described in Sec. 3.1, from the MCMC analysis discussed in Sec. 4.1 by considering all 8 redshift bins, removing the last bin and neglecting data from the last two bins.

There is a small impact in removing high-redshift information from the MCMC analysis for the LEDE₇ model: the parameters c_1 , c_2 and c_3 show a slight degradation in the constraints, while the best-fitting values are in agreement within the 2σ region. The same happens for the PLE analysis, except for the high-redshift parameters, which are severely degraded with the removal of the last two redshift bins (i.e. considering data between $0.68 < z < 3.5$), as it is expected since there is no constraining power at the high- z end, even though the fits are improved due to the fact that there are more data at low- z (which can also be seen by the decrease in the BIC value). We can also observe larger errors for the PLE+LEDE c_1, c_2, c_3 and c_a parameters, with a 2σ disagreement for c_1 and c_2 after removing the last two redshift bins (considering only the data between $0.68 < z < 3$). On the other hand, LEDE₈, LEDE₈₊₂ and LEDE₇₊₂ are reasonably insensitive to high-redshift information, showcasing similar constraints for the three redshift ranges considered.

In Figure 3, we show the best-fitting QLF from the corresponding MCMC analysis with all 8 redshift bins. Dashed lines mark the limiting magnitude cut $M_c = -25$ for the last redshift bin. When we consider all redshift bins and a constant magnitude cut for the dipole analysis, we neglect data contained in the shaded region. Discarding higher bins in the dipole analysis is equivalent to moving the dashed line and region of exclusion to fainter magnitudes.

Table 2. Best-fitting values for the parameters of the models described in Sec. 3.1, obtained from the MCMC analysis described in Sec. 4.1. The last column gives the Bayesian Information Criterion (BIC, Eq. 23) for each analysis.

| Model | z-range | Parameters | | | | BIC |
|-------|---------------|--------------------------|-------------------------|-------------------------|-------------------------|--------|
| PLE | 8 bins | $M_*(z_p)$ | $\log_{10} \Phi(z_p)$ | | | |
| | 0.68 – 4.0 | $-25.86^{+0.12}_{-0.12}$ | $-5.63^{+0.04}_{-0.05}$ | | | |
| | | a_l | b_l | $k_{1,l}$ | $k_{2,l}$ | 176.97 |
| | 0.68 – 2.2 | $-3.09^{+0.09}_{-0.10}$ | $-1.31^{+0.04}_{-0.04}$ | $-0.16^{+0.05}_{-0.05}$ | $-0.42^{+0.04}_{-0.04}$ | |
| | | a_h | b_h | $k_{1,h}$ | $k_{2,h}$ | |
| | 2.2 – 4.0 | $-2.46^{+0.05}_{-0.05}$ | $-1.10^{+0.07}_{-0.06}$ | $-0.42^{+0.07}_{-0.07}$ | $0.01^{+0.05}_{-0.05}$ | |
| | 7 bins | $M_*(z_p)$ | $\log_{10} \Phi(z_p)$ | | | |
| | 0.68 – 3.5 | $-25.82^{+0.13}_{-0.12}$ | $-5.62^{+0.05}_{-0.05}$ | | | |
| | | a_l | b_l | $k_{1,l}$ | $k_{2,l}$ | 171.88 |
| | 0.68 – 2.2 | $-3.06^{+0.09}_{-0.10}$ | $-1.29^{+0.04}_{-0.04}$ | $-0.16^{+0.05}_{-0.05}$ | $-0.42^{+0.04}_{-0.04}$ | |

Continued on next page

Table 2 – *Continued from previous page*

| | | | | | | |
|--|---------------|----------------------------------|----------------------------------|--------------------------------------|-------------------------------------|-------------------------|
| | 2.2 – 3.5 | a_h $-2.43^{+0.05}_{-0.06}$ | b_h $-1.09^{+0.07}_{-0.07}$ | $k_{1,h}$ $-0.47^{+0.10}_{-0.10}$ | $k_{2,h}$ $0.05^{+0.08}_{-0.08}$ | |
| | 6 bins | $M_*(z_p)$ | $\log_{10} \Phi(z_p)$ | | | |
| | 0.68 – 3.0 | $-25.63^{+0.14}_{-0.14}$ | $-5.53^{+0.05}_{-0.06}$ | | | |
| | | a_l | b_l | $k_{1,l}$ | $k_{2,l}$ | 151.77 |
| | 0.68 – 2.2 | $-2.93^{+0.09}_{-0.10}$ | $-1.21^{+0.05}_{-0.05}$ | $-0.09^{+0.06}_{-0.06}$ | $-0.37^{+0.04}_{-0.04}$ | |
| | | a_h | b_h | $k_{1,h}$ | $k_{2,h}$ | |
| | 2.2 – 3.0 | $-2.37^{+0.07}_{-0.07}$ | $-0.96^{+0.12}_{-0.10}$ | $-1.03^{+0.24}_{-0.26}$ | $0.90^{+0.34}_{-0.33}$ | |
| | 8 bins | $M_*(z_p)$ | $\log_{10} \Phi(z_p)$ | $\alpha(z_p)$ | β | |
| | 0.68 – 4.0 | $-25.52^{+0.16}_{-0.16}$ | $-5.48^{+0.06}_{-0.06}$ | $-2.80^{+0.08}_{-0.09}$ | $-1.16^{+0.06}_{-0.06}$ | |
| | | k_1 | k_2 | | | 175.50 |
| | 0.68 – 2.2 | $-0.10^{+0.05}_{-0.05}$ | $-0.38^{+0.04}_{-0.04}$ | | | |
| | | c_1 | c_2 | c_3 | c_a | |
| | 2.2 – 4.0 | $-0.62^{+0.06}_{-0.06}$ | $-0.06^{+0.05}_{-0.05}$ | $-0.67^{+0.13}_{-0.13}$ | $-0.01^{+0.11}_{-0.11}$ | |
| | 7 bins | $M_*(z_p)$ | $\log_{10} \Phi(z_p)$ | $\alpha(z_p)$ | β | |
| | 0.68 – 3.5 | $-25.53^{+0.16}_{-0.16}$ | $-5.47^{+0.06}_{-0.06}$ | $-2.80^{+0.09}_{-0.09}$ | $-1.15^{+0.07}_{-0.06}$ | |
| | | k_1 | k_2 | | | 163.30 |
| | 0.68 – 2.2 | $-0.08^{+0.05}_{-0.05}$ | $-0.37^{+0.04}_{-0.04}$ | | | |
| | | c_1 | c_2 | c_3 | c_a | |
| | 2.2 – 3.5 | $-0.73^{+0.07}_{-0.07}$ | $0.07^{+0.07}_{-0.07}$ | $-0.69^{+0.16}_{-0.15}$ | $0.09^{+0.13}_{-0.13}$ | |
| | 6 bins | $M_*(z_p)$ | $\log_{10} \Phi(z_p)$ | $\alpha(z_p)$ | β | |
| | 0.68 – 3.0 | $-25.58^{+0.16}_{-0.16}$ | $-5.47^{+0.06}_{-0.06}$ | $-2.84^{+0.09}_{-0.10}$ | $-1.16^{+0.07}_{-0.06}$ | |
| | | k_1 | k_2 | | | 140.38 |
| | 0.68 – 2.2 | $-0.03^{+0.06}_{-0.06}$ | $-0.34^{+0.04}_{-0.04}$ | | | |
| | | c_1 | c_2 | c_3 | c_a | |
| | 2.2 – 3.0 | $-1.08^{+0.12}_{-0.12}$ | $0.68^{+0.18}_{-0.18}$ | $-0.77^{+0.28}_{-0.26}$ | $0.36^{+0.22}_{-0.22}$ | |
| | 8 bins | $M_*(z_p)$ | $\log_{10} \Phi(z_p)$ | | | |
| | 0.68 – 4.0 | $-25.37^{+0.16}_{-0.16}$ | $-5.46^{+0.05}_{-0.05}$ | | | 169.05 |
| | | a | b | c_1 | c_2 | c_3 |
| | | $-2.66^{+0.07}_{-0.08}$ | $-1.03^{+0.08}_{-0.07}$ | $-0.43^{+0.01}_{-0.01}$ | $-0.30^{+0.01}_{-0.01}$ | $-0.96^{+0.04}_{-0.04}$ |
| | 7 bins | $M_*(z_p)$ | $\log_{10} \Phi(z_p)$ | | | |
| | 0.68 – 3.5 | $-25.40^{+0.16}_{-0.16}$ | $-5.47^{+0.05}_{-0.06}$ | | | 159.27 |
| | | a | b | c_1 | c_2 | c_3 |
| | | $-2.67^{+0.07}_{-0.08}$ | $-1.04^{+0.08}_{-0.07}$ | $-0.44^{+0.01}_{-0.01}$ | $-0.30^{+0.01}_{-0.01}$ | $-0.97^{+0.04}_{-0.04}$ |
| | 6 bins | $M_*(z_p)$ | $\log_{10} \Phi(z_p)$ | | | |
| | 0.68 – 3.0 | $-25.61^{+0.17}_{-0.17}$ | $-5.54^{+0.06}_{-0.06}$ | | | 130.82 |
| | | a | b | c_1 | c_2 | c_3 |
| | | $-2.74^{+0.08}_{-0.09}$ | $-1.10^{+0.07}_{-0.07}$ | $-0.49^{+0.02}_{-0.02}$ | $-0.32^{+0.01}_{-0.01}$ | $-1.08^{+0.04}_{-0.04}$ |
| | 8 bins | $M_*(z_p)$ | $\log_{10} \Phi(z_p)$ | | | |
| | 0.68 – 4.0 | $-26.17^{+0.16}_{-0.16}$ | $-5.77^{+0.06}_{-0.07}$ | | | 144.39 |
| | | c_1 | c_2 | c_3 | | |
| | | $-0.94^{+0.06}_{-0.06}$ | $-0.4^{+0.02}_{-0.02}$ | $-1.99^{+0.1}_{-0.1}$ | | |
| | | $a(z_p)$ | c_a | $b(z_p)$ | c_b | |
| | | $-2.84^{+0.08}_{-0.09}$ | $-0.16^{+0.07}_{-0.07}$ | $-1.33^{+0.05}_{-0.05}$ | $-0.5^{+0.04}_{-0.04}$ | |
| | 7 bins | $M_*(z_p)$ | $\log_{10} \Phi(z_p)$ | | | |
| | 0.68 – 3.5 | $-26.16^{+0.16}_{-0.16}$ | $-5.76^{+0.07}_{-0.07}$ | | | 137.44 |
| | | c_1 | c_2 | c_3 | | |
| | | $-0.92^{+0.06}_{-0.07}$ | $-0.39^{+0.02}_{-0.02}$ | $-1.95^{+0.11}_{-0.11}$ | | |

Continued on next page

Table 2 – *Continued from previous page*

| | | | | | | | |
|---------------------------|--------------------------|--------------------------|-------------------------|-------------------------|-------------------------|-------------------------|------------------------|
| | | $a(z_p)$ | c_a | $b(z_p)$ | c_b | | |
| | | $-2.84^{+0.08}_{-0.09}$ | $-0.14^{+0.07}_{-0.07}$ | $-1.33^{+0.05}_{-0.05}$ | $-0.47^{+0.05}_{-0.05}$ | | |
| | 6 bins | $M_*(z_p)$ | $\log_{10} \Phi(z_p)$ | | | | |
| | | $-26.18^{+0.18}_{-0.17}$ | $-5.77^{+0.07}_{-0.07}$ | | | | |
| | | c_1 | c_2 | c_3 | | 119.68 | |
| | 0.68 – 3.0 | $-0.87^{+0.08}_{-0.08}$ | $-0.38^{+0.02}_{-0.02}$ | $-1.84^{+0.14}_{-0.13}$ | | | |
| | | $a(z_p)$ | c_a | $b(z_p)$ | c_b | | |
| | | $-2.85^{+0.09}_{-0.10}$ | $-0.09^{+0.06}_{-0.06}$ | $-1.33^{+0.06}_{-0.05}$ | $-0.4^{+0.06}_{-0.06}$ | | |
| LEDE₈ | 8 bins | $M_*(z_p)$ | $\log_{10} \Phi(z_p)$ | | | | |
| | | $-25.72^{+0.16}_{-0.16}$ | $-5.56^{+0.06}_{-0.06}$ | | | 141.64 | |
| | | a | b | c_1 | c_2 | c_3 | c_4 |
| | 0.68 – 4.0 | $-2.79^{+0.08}_{-0.09}$ | $-1.10^{+0.07}_{-0.06}$ | $-0.37^{+0.01}_{-0.01}$ | $-0.20^{+0.01}_{-0.01}$ | $-0.78^{+0.04}_{-0.04}$ | $0.34^{+0.04}_{-0.04}$ |
| | | $M_*(z_p)$ | $\log_{10} \Phi(z_p)$ | | | | |
| | | $-25.72^{+0.16}_{-0.16}$ | $-5.56^{+0.06}_{-0.06}$ | | | 133.70 | |
| | | a | b | c_1 | c_2 | c_3 | c_4 |
| | 0.68 – 3.5 | $-2.79^{+0.08}_{-0.09}$ | $-1.10^{+0.07}_{-0.06}$ | $-0.37^{+0.02}_{-0.02}$ | $-0.20^{+0.02}_{-0.02}$ | $-0.75^{+0.04}_{-0.05}$ | $0.38^{+0.05}_{-0.05}$ |
| | | $M_*(z_p)$ | $\log_{10} \Phi(z_p)$ | | | | |
| | | $-25.75^{+0.17}_{-0.16}$ | $-5.58^{+0.06}_{-0.06}$ | | | 118.76 | |
| | | a | b | c_1 | c_2 | c_3 | c_4 |
| | 0.68 – 3.0 | $-2.80^{+0.08}_{-0.09}$ | $-1.12^{+0.07}_{-0.06}$ | $-0.40^{+0.02}_{-0.02}$ | $-0.22^{+0.02}_{-0.02}$ | $-0.75^{+0.07}_{-0.07}$ | $0.38^{+0.07}_{-0.07}$ |
| LEDE₈₊₂ | 8 bins | $M_*(z_p)$ | $\log_{10} \Phi(z_p)$ | | | | |
| | | $-25.92^{+0.20}_{-0.20}$ | $-5.65^{+0.08}_{-0.09}$ | | | 147.19 | |
| | | c_1 | c_2 | c_3 | c_4 | | |
| | 0.68 – 4.0 | $-0.50^{+0.09}_{-0.19}$ | $-0.21^{+0.02}_{-0.06}$ | $-1.04^{+0.22}_{-0.42}$ | $0.32^{+0.06}_{-0.11}$ | | |
| | | $a(z_p)$ | c_a | $b(z_p)$ | c_b | | |
| | | $-2.83^{+0.09}_{-0.10}$ | $-0.01^{+0.09}_{-0.11}$ | $-1.22^{+0.08}_{-0.08}$ | $-0.17^{+0.09}_{-0.17}$ | | |
| | | $M_*(z_p)$ | $\log_{10} \Phi(z_p)$ | | | | |
| | | $-25.90^{+0.20}_{-0.20}$ | $-5.64^{+0.08}_{-0.08}$ | | | 138.06 | |
| | | c_1 | c_2 | c_3 | c_4 | | |
| | 0.68 – 3.5 | $-0.48^{+0.09}_{-0.14}$ | $-0.21^{+0.02}_{-0.04}$ | $-0.99^{+0.23}_{-0.30}$ | $0.35^{+0.06}_{-0.08}$ | | |
| | | $a(z_p)$ | c_a | $b(z_p)$ | c_b | | |
| | | $-2.81^{+0.09}_{-0.10}$ | $0.02^{+0.10}_{-0.10}$ | $-1.21^{+0.08}_{-0.08}$ | $-0.17^{+0.09}_{-0.12}$ | | |
| | $M_*(z_p)$ | $\log_{10} \Phi(z_p)$ | | | | | |
| | $-25.95^{+0.23}_{-0.21}$ | $-5.67^{+0.09}_{-0.09}$ | | | 118.97 | | |
| | c_1 | c_2 | c_3 | c_4 | | | |
| 0.68 – 3.0 | $-0.55^{+0.11}_{-0.12}$ | $-0.24^{+0.03}_{-0.04}$ | $-1.06^{+0.29}_{-0.29}$ | $0.33^{+0.09}_{-0.09}$ | | | |
| | $a(z_p)$ | c_a | $b(z_p)$ | c_b | | | |
| | $-2.80^{+0.11}_{-0.12}$ | $0.05^{+0.11}_{-0.12}$ | $-1.24^{+0.08}_{-0.07}$ | $-0.20^{+0.09}_{-0.09}$ | | | |

REFERENCES

- Ade, P. A. R., Aghanim, N., Arnaud, M., et al. 2016, *A&A*, 594, A7, doi: [10.1051/0004-6361/201525830](https://doi.org/10.1051/0004-6361/201525830)
- Aghanim, N., Akrami, Y., Arroja, F., et al. 2020, *Astronomy & Astrophysics*, 641, A1, doi: [10.1051/0004-6361/201833880](https://doi.org/10.1051/0004-6361/201833880)
- Alonso, D., Bull, P., Ferreira, P. G., Maartens, R., & Santos, M. G. 2015, *The Astrophysical Journal*, 814, 145, doi: [10.1088/0004-637X/814/2/145](https://doi.org/10.1088/0004-637X/814/2/145)
- Bengaly, C. A., Maartens, R., & Santos, M. G. 2018, *Journal of Cosmology and Astroparticle Physics*, 2018, 031, doi: [10.1088/1475-7516/2018/04/031](https://doi.org/10.1088/1475-7516/2018/04/031)

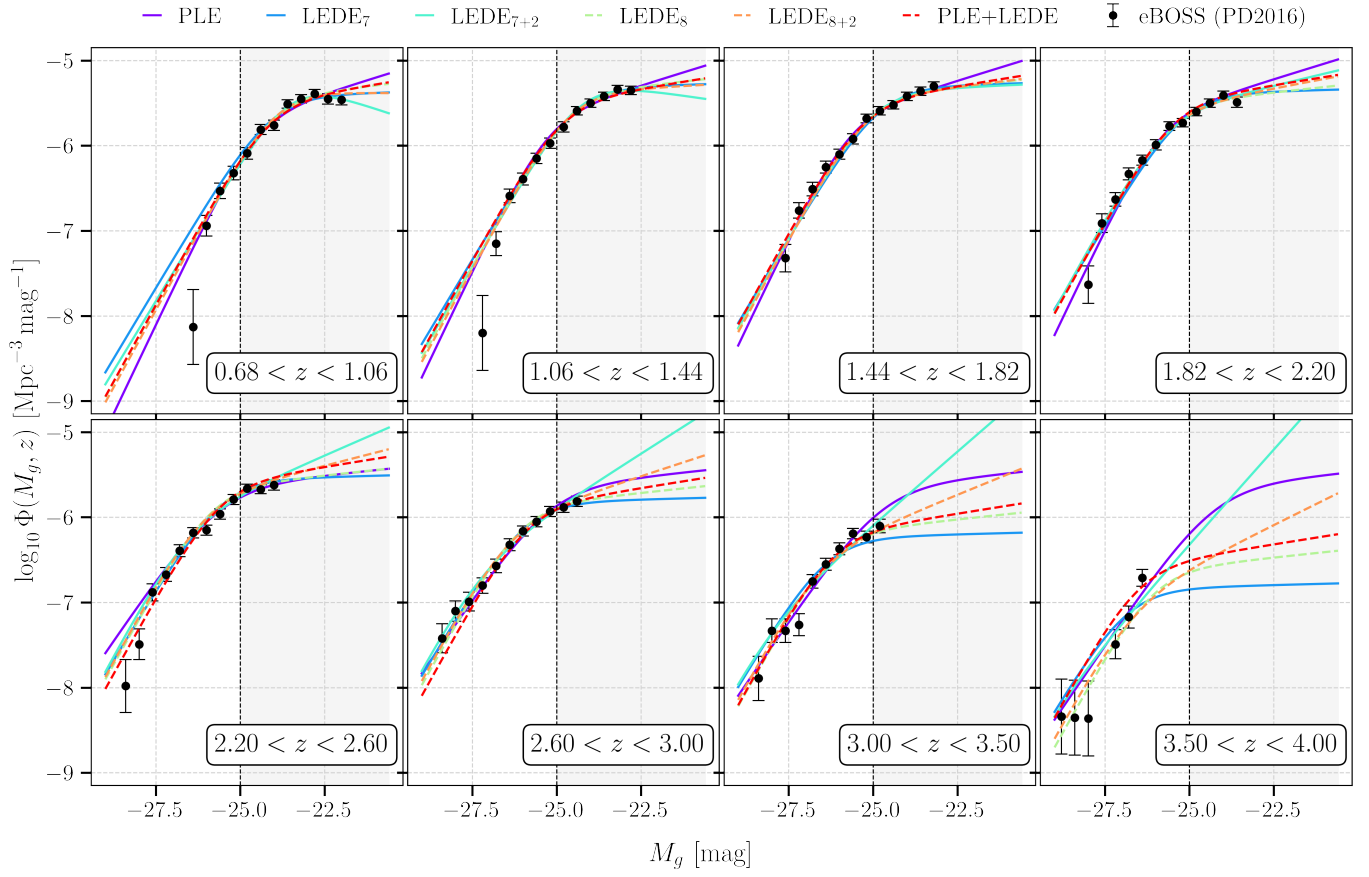


Figure 3. Best-fitting quasar luminosity functions for the models described in Sec. 3.1. The corresponding best-fitting parameters are shown in Table 2. The data points and uncertainties are taken from PD2016. Dashed line separates the region below the limiting magnitude cut $M_c = -25$ for the last redshift bin (Wang et al. 2020). The shaded region is neglected when we consider all 8 redshift bins for the dipole analysis.

Bengaly, C. A., Siewert, T. M., Schwarz, D. J., & Maartens, R. 2019, *Monthly Notices of the Royal Astronomical Society*, 486, 1350, doi: [10.1093/mnras/stz832](https://doi.org/10.1093/mnras/stz832)

Blake, C., & Wall, J. 2002, arXiv preprint astro-ph/0203385, doi: [10.1038/416150a](https://doi.org/10.1038/416150a)

Blas, D., Lesgourgues, J., & Tram, T. 2011, *JCAP*, 2011, 034–034, doi: [10.1088/1475-7516/2011/07/034](https://doi.org/10.1088/1475-7516/2011/07/034)

Bonvin, C., & Durrer, R. 2011, *Phys. Rev. D*, 84, 063505, doi: [10.1103/PhysRevD.84.063505](https://doi.org/10.1103/PhysRevD.84.063505)

Boyle, B. J., Shanks, T., Croom, S., et al. 2000, *Monthly Notices of the Royal Astronomical Society*, 317, 1014, doi: [10.1046/j.1365-8711.2000.03730.x](https://doi.org/10.1046/j.1365-8711.2000.03730.x)

Carballo, R., González-Serrano, J. I., Benn, C. R., Sánchez, S. F., & Vigotti, M. 1999, *Monthly Notices of the Royal Astronomical Society*, 306, 137, doi: [10.1023/A:1002189323147](https://doi.org/10.1023/A:1002189323147)

Challinor, A., & Lewis, A. 2011, *Physical Review D*, 84, 043516, doi: [10.1103/PhysRevD.84.043516](https://doi.org/10.1103/PhysRevD.84.043516)

Clarkson, C. 2012, *Comptes Rendus Physique*, 13, 682, doi: [10.1016/j.crchy.2012.04.005](https://doi.org/10.1016/j.crchy.2012.04.005)

Clarkson, C., & Maartens, R. 2010, *Class. Quant. Grav.*, 27, 124008, doi: [10.1088/0264-9381/27/12/124008](https://doi.org/10.1088/0264-9381/27/12/124008)

Colin, J., Mohayaee, R., Rameez, M., & Sarkar, S. 2017, *Monthly Notices of the Royal Astronomical Society*, 471, 1045, doi: [10.1093/mnras/stx1631](https://doi.org/10.1093/mnras/stx1631)

Croom, S. M., Smith, R., Boyle, B., et al. 2004, *Monthly Notices of the Royal Astronomical Society*, 349, 1397, doi: [10.1111/j.1365-2966.2004.07619.x](https://doi.org/10.1111/j.1365-2966.2004.07619.x)

Croom, S. M., Richards, G. T., Shanks, T., et al. 2009, *Monthly Notices of the Royal Astronomical Society*, 399, 1755, doi: [10.1111/j.1365-2966.2009.15398.x](https://doi.org/10.1111/j.1365-2966.2009.15398.x)

Dalang, C., & Bonvin, C. 2022, *Monthly Notices of the Royal Astronomical Society*, 512, 3895, doi: [10.1093/mnras/stac726](https://doi.org/10.1093/mnras/stac726)

Ehlers, J., Geren, P., & Sachs, R. K. 1968, *Journal of Mathematical Physics*, 9, 1344, doi: [10.1063/1.1664720](https://doi.org/10.1063/1.1664720)

Ellis, G., & Baldwin, J. 1984, *Monthly Notices of the Royal Astronomical Society*, 206, 377, doi: [10.1093/mnras/206.2.377](https://doi.org/10.1093/mnras/206.2.377)

- Ellis, G., Treciokas, R., & Matrauers, D. 1983, *Annals of Physics*, 150, 487, doi: [10.1016/0003-4916\(83\)90024-6](https://doi.org/10.1016/0003-4916(83)90024-6)
- Foreman-Mackey, D., Hogg, D. W., Lang, D., & Goodman, J. 2013, *PASP*, 125, 306, doi: [10.1086/670067](https://doi.org/10.1086/670067)
- Ghosh, S., Jain, P., Kashyap, G., et al. 2016, *Journal of Astrophysics and Astronomy*, 37, 1, doi: [10.1007/s12036-016-9395-8](https://doi.org/10.1007/s12036-016-9395-8)
- Gibelyou, C., & Huterer, D. 2012, *Monthly Notices of the Royal Astronomical Society*, 427, 1994, doi: [10.1111/j.1365-2966.2012.22032.x](https://doi.org/10.1111/j.1365-2966.2012.22032.x)
- Harris, C. R., Millman, K. J., van der Walt, S. J., et al. 2020, *Nature*, 585, 357, doi: [10.1038/s41586-020-2649-2](https://doi.org/10.1038/s41586-020-2649-2)
- Hunter, J. D. 2007, *Computing in Science & Engineering*, 9, 90, doi: [10.1109/MCSE.2007.55](https://doi.org/10.1109/MCSE.2007.55)
- Liddle, A. R. 2004, *Monthly Notices of the Royal Astronomical Society*, 351, L49, doi: [10.1111/j.1365-2966.2004.08033.x](https://doi.org/10.1111/j.1365-2966.2004.08033.x)
- Maartens, R., Clarkson, C., & Chen, S. 2018, *Journal of Cosmology and Astroparticle Physics*, 2018, 013, doi: [10.1088/1475-7516/2018/01/013](https://doi.org/10.1088/1475-7516/2018/01/013)
- Maartens, R., Fonseca, J., Camera, S., et al. 2021, *Journal of Cosmology and Astroparticle Physics*, 2021, 009, doi: [10.1088/1475-7516/2021/12/009](https://doi.org/10.1088/1475-7516/2021/12/009)
- Nadolny, T., Durrer, R., Kunz, M., & Padmanabhan, H. 2021, *Journal of Cosmology and Astroparticle Physics*, 2021, 009, doi: [10.1088/1475-7516/2021/11/009](https://doi.org/10.1088/1475-7516/2021/11/009)
- Palanque-Delabrouille, N., Yèche, C., Myers, A., et al. 2011, *Astronomy & Astrophysics*, 530, A122, doi: [10.1051/0004-6361/201016254](https://doi.org/10.1051/0004-6361/201016254)
- Palanque-Delabrouille, N., Magneville, C., Yèche, C., et al. 2016, *Astronomy & Astrophysics*, 587, A41, doi: [10.1051/0004-6361/201527392](https://doi.org/10.1051/0004-6361/201527392)
- Peebles, P., & Wilkinson, D. T. 1968, *Physical Review*, 174, 2168, doi: [10.1103/PhysRev.174.2168](https://doi.org/10.1103/PhysRev.174.2168)
- Pozzetti, L., Hirata, C., Geach, J., et al. 2016, *Astronomy & Astrophysics*, 590, A3, doi: [10.1051/0004-6361/201527081](https://doi.org/10.1051/0004-6361/201527081)
- Rasera, Y., Breton, M.-A., Corasaniti, P.-S., et al. 2022, *Astronomy & Astrophysics*, 661, A90, doi: [10.1051/0004-6361/202141908](https://doi.org/10.1051/0004-6361/202141908)
- Ross, N. P., McGreer, I. D., White, M., et al. 2013, *The Astrophysical Journal*, 773, 14, doi: [10.1088/0004-637X/773/1/14](https://doi.org/10.1088/0004-637X/773/1/14)
- Rubart, M., & Schwarz, D. J. 2013, *Astronomy & Astrophysics*, 555, A117, doi: [10.1051/0004-6361/201321215](https://doi.org/10.1051/0004-6361/201321215)
- Schmidt, K. B., Marshall, P. J., Rix, H.-W., et al. 2010, *The Astrophysical Journal*, 714, 1194, doi: [10.1088/0004-637X/714/2/1194](https://doi.org/10.1088/0004-637X/714/2/1194)
- Secrest, N. J., von Hausegger, S., Rameez, M., Mohayaee, R., & Sarkar, S. 2022, *The Astrophysical Journal Letters*, 937, L31, doi: [10.3847/2041-8213/ac88c0](https://doi.org/10.3847/2041-8213/ac88c0)
- Secrest, N. J., von Hausegger, S., Rameez, M., et al. 2021, *The Astrophysical journal letters*, 908, L51, doi: [10.3847/2041-8213/abdd40](https://doi.org/10.3847/2041-8213/abdd40)
- Stewart, J., & Sciamia, D. 1967, *Nature*, 216, 748, doi: [10.1038/216748a0](https://doi.org/10.1038/216748a0)
- Stoeger, W. R., Maartens, R., & Ellis, G. 1995, *The Astrophysical Journal*, 443, 1, doi: [10.1086/175496](https://doi.org/10.1086/175496)
- Tiwari, P., Kothari, R., Naskar, A., Nadkarni-Ghosh, S., & Jain, P. 2015, *Astroparticle Physics*, 61, 1, doi: [10.1016/j.astropartphys.2014.06.004](https://doi.org/10.1016/j.astropartphys.2014.06.004)
- Tiwari, P., & Nusser, A. 2016, *Journal of Cosmology and Astroparticle Physics*, 2016, 062, doi: [10.1088/1475-7516/2016/03/062](https://doi.org/10.1088/1475-7516/2016/03/062)
- Virtanen, P., Gommers, R., Oliphant, T. E., et al. 2020, *Nature Methods*, 17, 261, doi: [10.1038/s41592-019-0686-2](https://doi.org/10.1038/s41592-019-0686-2)
- Wang, M. S., Beutler, F., & Bacon, D. 2020, *Monthly Notices of the Royal Astronomical Society*, 499, 2598, doi: [10.1093/mnras/staa2998](https://doi.org/10.1093/mnras/staa2998)